The influence of different species of gases on the luminescent and structural properties of pulsed laser-ablated Y2O2S:Eu3+ thin films

Article *in* Applied Physics A · May 2016

DOI: 10.1007/s00339-016-0062-3

3 authors:

Abdub Guyo Ali

University of the Free State

6 PUBLICATIONS **19** CITATIONS

SEE PROFILE

H. C. Swart

University of the Free State

528 PUBLICATIONS **3,327** CITATIONS

SEE PROFILE

F. B. Dejene

University of the Free State

94 PUBLICATIONS **331** CITATIONS

SEE PROFILE

Appl. Phys. A (2016)122:534
DOI 10.1007/s00339-016-0062-3

Applied Physics A
Materials Science & Processing

The influence of different species of gases on the luminescent and structural properties of pulsed laser-ablated $Y_2O_2S:Eu^{3+}$ thin films

A. G. Ali[1] · B. F. Dejene[1] · H. C. Swart[2]

Received: 15 October 2015 / Accepted: 15 April 2016

Abstract $Y_2O_2S:Eu^{3+}$ films have been grown on Si (100) substrates by using a pulsed laser deposition technique. The thin films grown under vacuum, argon and oxygen ambient have been characterized using structural and luminescent measurements. The X-ray diffraction patterns showed mixed phases of cubic and hexagonal crystal structures. The crystallinity of the film deposited in vacuum is poor, but improved significantly in argon and oxygen atmosphere. Similarly, both scanning electron microscopy and atomic force microscopy confirmed that different species of gases affected the morphology of the films. The average band gap of the films calculated from diffuse reflectance spectra using the Kubelka–Munk function was about 4.69 eV. The photoluminescence measurements indicated red emission of $Y_2O_2S:Eu^{3+}$ thin films with the most intense peak appearing at 612 nm, which is assigned to the $^5D_0$–$^7F_2$ transition of Eu^{3+}. The intensities of this most intense peak greatly depend on the species of gas with argon having the highest peak. This phosphor has applications in the flat panel displays.

1 Introduction

Nanostructure materials are being actively explored nowadays because of their size-induced novel characteristics and applications ranging from microtips to optoelectronics. To exploit the optical properties of these materials and to meet the ever—increasing demands of energy, tremendous emphasis is being placed on alternate sources of energy conservation and low-power-driven display devices. Afterglow phosphors are materials that are readily excited by ambient lights and continuously radiate visible light for many hours at high brightness levels [1]. Nanoscale $Y_2O_2S:Eu^{3+}$ has remarkably different luminescent properties from those of bulk samples such as emission line broadening, lifetime changes and its spectral shift [2]. There are several methods to synthesize nanocrystalline $Y_2O_2S:Eu^{3+}$, such as sol–gel [3], combustion [4], microemulsion [5] and spray pyrolysis method [6], but these methods are limited in the complexity of the preparation methods. Solid-state reaction at room temperature is a good method to synthesize nanoparticles [7–9]. Recently, the pulsed laser deposition (PLD) technique, which provides a unique process for stoichiometric evaporation of target materials and control of film morphology [10, 11], has been used for the deposition of oxysulfide films [12–14]. In most of the reported works [15–17], the $Y_2O_2S:Eu^{3+}$ phosphors have been prepared and investigated in the form of powders. However, for various industrial applications such as device fabrication and surface coatings, it is also important to investigate the performance of these phosphors in the form of thin films. Moreover, it is well documented that thin-film phosphors have several advantages over powders, such as higher lateral resolution from smaller grains, better thermal stability, reduced out gassing and better adhesion to solid substrates [18]. Among the techniques used to prepare luminescent thin films, PLD has several attractive features, including stoichiometric transfer of the target material, generation of quality plume of energetic species, hyper-thermal reaction between the ablated cations and molecular gas in the ablation plasma

✉ A. G. Ali
aliag@ufs.ac.za

[1] Department of Physics, University of the Free State (Qwaqwa Campus), Private Bag X13, Phuthaditjhaba 9866, South Africa

[2] Department of Physics, University of the Free State, P.O. Box 339, Bloemfontein 9300, South Africa

Published online: 27 April 2016

and compatibility with background pressures ranging from UHV to 100 Pa [19]. The plasma fabricated during pulsed laser ablation is very energetic, and its mobility can be easily controlled by changing processing parameters [20]. The presence of a background gas in the chamber has a strong influence on the quality of the plasma produced by the laser. The gas can modify the kinetic energy and the spatial distribution of the ejected species present in the plasma, and it may also induce compositional changes in the deposited films [21]. Plume collisions may also provide an increase in the vibrational energy of molecular species [22]. Thus, the gas affects the spatial distribution, the deposition rate, the energy and distribution of ablated particles, thereby controlling the cluster formation, cluster size, cluster energy and particle distribution [23]. Dauscher et al. [24] investigated the influence of argon atmosphere on the microstructural properties of $Ca_xCO_4Sb_{12}$ films prepared by pulsed laser deposition and found that the films deposited in argon atmosphere were more delaminated than those prepared in vacuum. The report from Supab et al. [25] on laser-ablated ZnO nanorods showed that the growth rate of nanostructures in oxygen atmosphere was slower than in argon atmosphere.

In the current work, we report on the influence of vacuum, argon and oxygen atmospheres on the morphology, structural and photoluminescence (PL) properties of pulsed laser-deposited (PLD) $Y_2O_2S:Eu^{3+}$ thin films. A detailed report on the influence of working atmosphere on the properties of the pulsed laser-deposited $Y_2O_2S:Eu^{3+}$ thin films is presented.

2 Experimental procedures

2.1 Powder preparation

Eu^{3+}-doped yttrium oxysulfide nanocrystals were synthesized using the sol–combustion route. The method of synthesis essentially comprises of mixing the precursors in appropriate stoichiometric ratios, followed by firing in an air tube furnace at a temperature of 400 °C. The stoichiometric ratio between the fuel (thiourea) and the flux (ethanol) is very important otherwise yttrium oxide formation is inevitable. The white foamy product was then ground and left to dry in an enclosed oven for 24 h.

2.2 Pulsed laser deposition (PLD)

The Si (100) wafers used as substrate were first chemical cleaned. The powder was pressed without binders to prepare a pellet that was used as an ablation target. The target was annealed at 700 °C for 12 h in air to remove water vapor and other volatile compounds that might be trapped in the pellet before placing it on the target holder of the PLD system. The deposition chamber was evacuated to a base pressure of 8.2×10^{-6} mTorr. The Lambda Physic 248-nm KrF excimer laser was used to ablate the phosphor pellet in vacuum, argon and oxygen atmospheres. A Baratron Direct (Gas Independent) Pressure/Vacuum capacitance Manometer (1.33×10^{-2} mTorr) was used for the 50 mtorr pressure measurements. The laser energy density, number of pulses and laser frequency were set to 0.74 J/cm^2, 12,000 and 10 Hz, respectively. The substrate temperature was fixed at 300 °C, and the target to substrate distance was 5 cm. The ablated area was 1 cm^2.

2.3 Characterization

The Shimadzu Superscan SSX-550 system was used to collect the scanning electron microscopy (SEM) micrographs. Atomic force microscopy (AFM) micrographs were obtained from the Shimadzu SPM—9600 model. X-ray diffraction (XRD) data were collected by using a SIEMENS D5000 diffractometer using CuKα radiation of $\lambda = 1.5405$ nm. PL excitation and emission spectra were recorded using a Cary Eclipse fluorescence spectrophotometer (Model: LS 55) with a built-in xenon lamp and a grating to select a suitable wavelength for excitation. The excitation wavelength was 230 nm, and the slit width was 10 nm. The afterglow curves for the films were also obtained with the Cary Eclipse spectrophotometer.

3 Results and discussion

3.1 X-ray diffraction analysis

Figure 1 shows the XRD patterns of $Y_2O_2S:Eu^{3+}$ thin films grown at 300 °C in vacuum, argon and oxygen atmospheres. The patterns show mixed phases of cubic and hexagonal crystal structures. The film grown in O_2 atmosphere has a cubic phase, while that grown in vacuum and argon atmospheres are hexagonal. The average lattice parameters for the hexagonal phase $a = 3.785$ nm and $c = 6.589$ nm are very close to the standard values provided in the powder diffraction file PDF # 89-1397. The average lattice parameter for the cubic phase is 6.026 nm, which is in agreement with the standard JCPDS CARD No. 83-0927 [26]. The intensities of the XRD peaks were found to increase in the order argon, vacuum and oxygen. This may be attributed to the enhanced oxidation kinetics and improvement in crystalline nature of the films. It is also clear that the thin film consists of both nanoparticles and microparticles as seen from the narrow and broad XRD peaks. The crystallite size of the films with hexagonal and cubic phase ranging between 80 and 480 nm was estimated by using Eqs. (1) and (2), respectively;

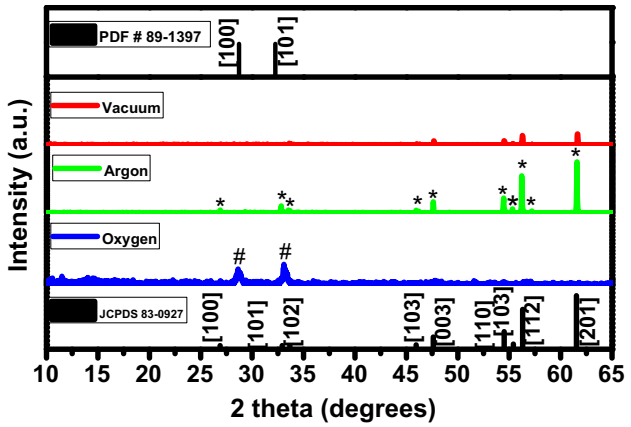

Fig. 1 XRD spectra of the $Y_2O_2S:Eu^{3+}$ thin films deposited in vacuum and different gas atmospheres

$$\frac{1}{d^2} = \frac{4(h^2 + k^2 + hk)}{3a^2} + \frac{l^2}{c^2} \quad (1)$$

$$\frac{1}{d^2} = \frac{h^2 + k^2 + l^2}{a^2} \quad (2)$$

There is a marginal decrease (−0.17 %) in crystallographic unit cell that tends to contract due to the increase in surface area of the layers for the $Y_2O_2S:Eu^{3+}$ nanostructures. This may lead to a decrease in the lattice constant. Eu_2O_3 diffraction peaks from XRD patterns were not detected, indicating that the Eu^{3+} was incorporated into the Y_2O_2S host lattice homogeneously.

3.2 Scanning electron microscopy (SEM)

Figure 2 shows the SEM pictures of the films prepared in different working atmospheres. The size of the particles obtained from the SEM images is different from the size obtained via XRD pattern. This is owing to the fact that XRD patterns give the information about the crystallite size. The crystallites are the grain arranges in a particular orientation of crystal plane [27]. The film deposited in vacuum, shown in Fig. 2a, had a smooth surface with numerous bigger spherical particles. The film deposited in Ar atmosphere (Fig. 3b) had a much rougher surface packed with larger number of spherical particles than that of the film deposited in the O_2 atmosphere. The film that was deposited in the O_2 atmosphere, in Fig. 3c, had a rougher surface with small cracks on the surface. The crystallite sizes as shown by SEM micrographs consist of both nano- and microparticles. The SEM micrographs show that the surfaces of the films prepared in the gas atmosphere are much rougher than that deposited in vacuum. The increase in surface roughness in the O_2 and Ar

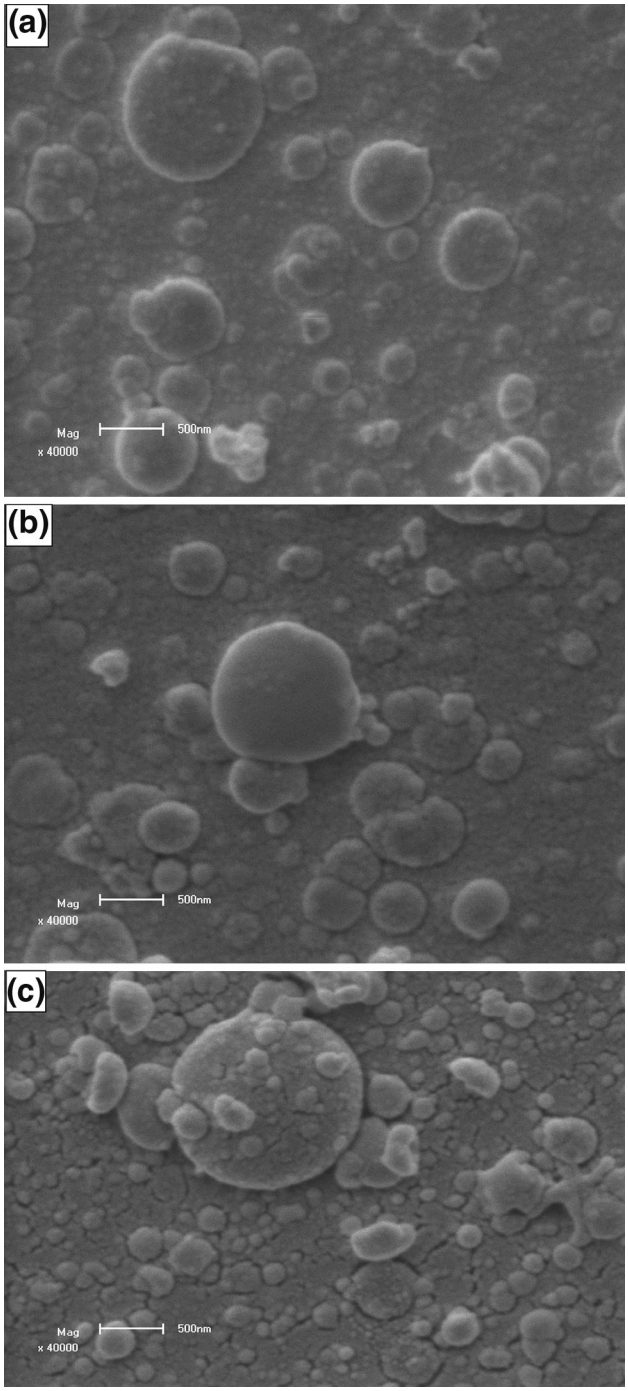

Fig. 2 SEM micrographs for thin films deposited in **a** vacuum, **b** argon and **c** oxygen atmosphere

atmospheres is due to the enhanced particulate formation in the plume, which is a typical characteristic of high-pressure laser ablation [28].

3.3 Atomic force microscopy (AFM)

Figure 3 show AFM images of the samples deposited in (a) vacuum, (b) argon and (c) oxygen atmosphere. It is

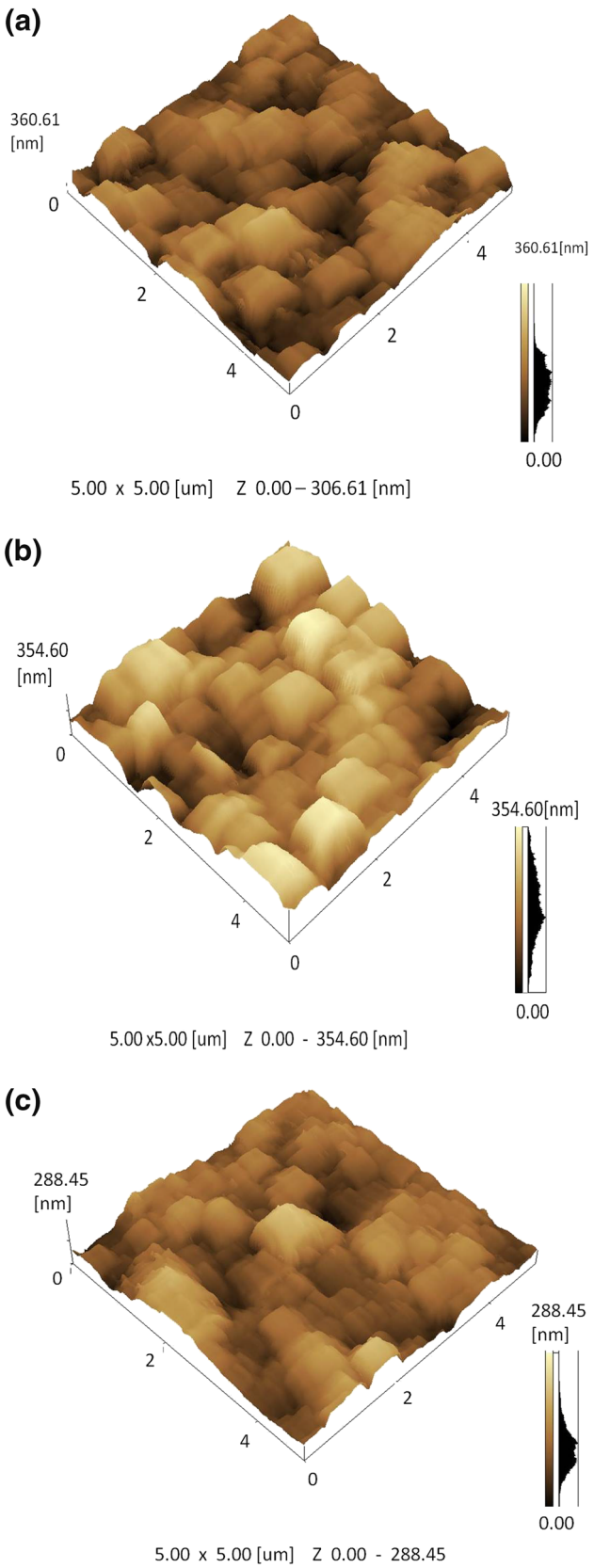

Fig. 3 AFM images of thin films deposited in **a** vacuum, **b** argon and **c** oxygen atmospheres

clear that almost hexagonally shaped nanoparticles were deposited during the deposition process. The particles were also less agglomerated for films grown in gas atmospheres (Figs. 3b vs. 4c). In vacuum, the plume does not undergo scattering (collisions) due to gas particles; hence, the arrival of the particle is more compared to case of argon and oxygen and thus higher PL intensity. Argon being a heavier gas scatters more particles as compared to oxygen; however, the speed of argon particles is less than those of oxygen. The arrival of the particles is higher in case of oxygen, hence intensity.

Collisions between the vaporized particles close to the target in the case of films deposited in gas atmosphere lead to nucleation and growth of smaller nanoparticles when arriving at the substrate. In vacuum, there are virtually no collisions between the particles before reaching the substrate. Longer residence time of the particles in the plume, as is the case of films deposited in gas atmosphere, leads to more evenly distributed particles (Fig. 3c). Light emission from the spherical-shaped phosphor particles as excited by the electron beam is more intense due to the fact that much less photons encounter total internal reflection [29, 30]. The increase in the deposition pressure is reported to have caused an increase in the connectivity (agglomeration) between particles due to sintering of small particles [31]. This would eventually lead to grain growth at high enough pressure. In this case, we also found that more agglomeration occurred during deposition in gas atmosphere than in vacuum.

3.4 Photoluminescence results

Figure 4a indicates the excitation spectra of $Y_2O_2S:Eu^{3+}$ thin films grown under vacuum, argon and oxygen atmosphere. Excitation spectra were recorded keeping the emission wavelength at 612 nm. The figure indicates intense excitation spectra for the sample deposited in vacuum followed by that deposited in argon. The sample deposited in oxygen atmosphere (inset) shows no clear visible excitation peak. These spectra consist of two charge transfer bands (CTBs). The band located at 237 nm is due to $O^{2-} \rightarrow Eu^{3+}$ CTB, while that at 312 nm is due to $Eu^{3+} \rightarrow S^{2-}$ CTB.

Figure 4b shows the deconvulated excitation spectra of $Y_2O_2S:Eu^{3+}$ thin films deposited in vacuum, argon and oxygen. The figure indicates two transitions at 237 and 312 nm wavelengths. The transition located at 237 nm is due to charge transfer band between O^{2-} and Eu^{3+} ions, while that located at 312 and 315 nm is associated with $Eu^{3+} \rightarrow S2^{-}$ charge transfer band.

Figure 4c, d shows excitation wavelengths for films deposited in different atmospheres. In each case, the excitation wavelengths were found at different emission

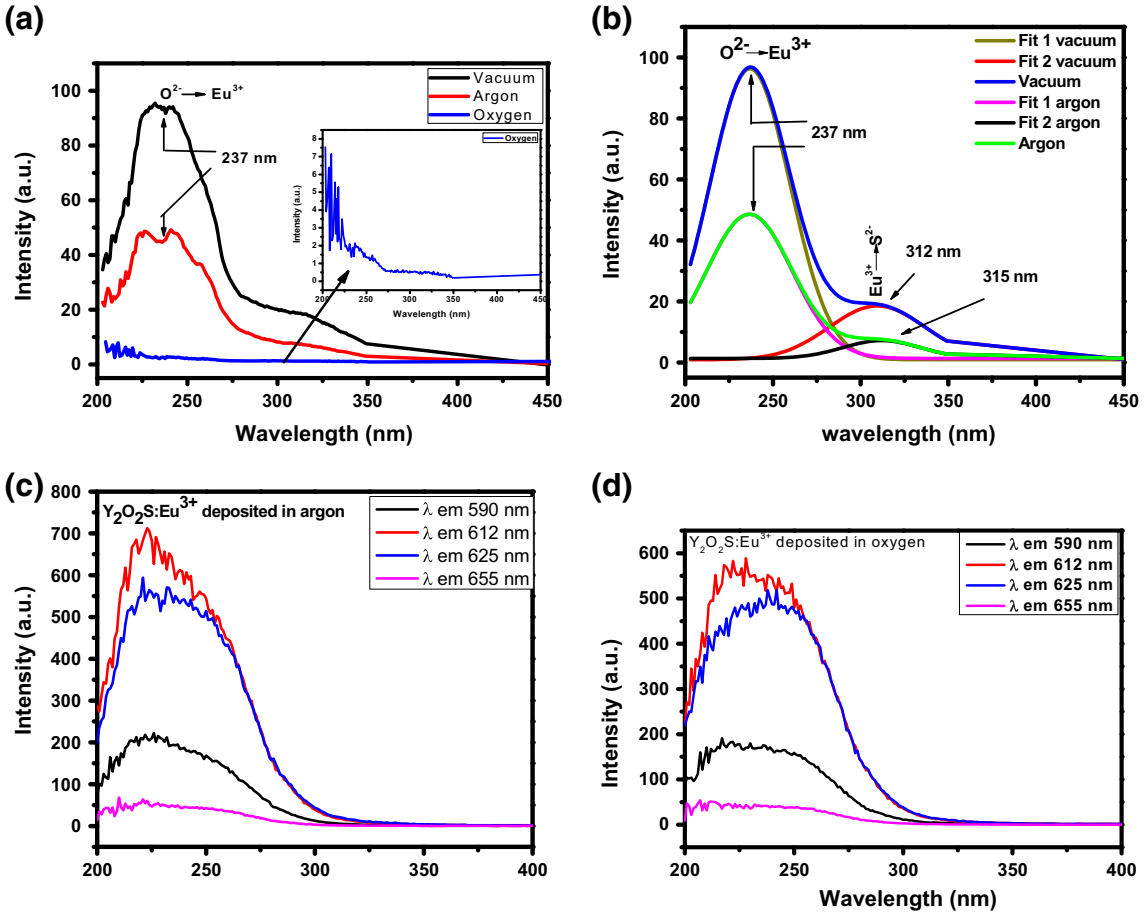

Fig. 4 **a** Excitation spectra for $Y_2O_2S:Eu^{3+}$ thin films deposited in vacuum, argon and oxygen atmosphere at emission wavelength of 612 nm. *Inset* Excitation spectrum for sample deposited in oxygen atmosphere. **b** Deconvoluted excitation spectra for $Y_2O_2S:Eu^{3+}$ thin films deposited in vacuum, argon and oxygen atmosphere. **c** Excitation spectra of $Y_2O_2S:Eu^{3+}$ thin film deposited in argon recorded at 590, 612, 625 and 655 nm emission wavelengths. **d** Excitation spectra of $Y_2O_2S:Eu^{3+}$ thin film deposited in oxygen recorded at 590, 612, 625 and 655 nm emission wavelengths

wavelengths in order to find the best excitation for every film. Figure 4c indicates excitation wavelengths for the film deposited in argon atmosphere. The best excitation wavelength was achieved when the emission wavelength was at 612 nm, followed by 625 and 590 nm, respectively. The excitation wavelength with the least intensity is achieved at 655 nm emission wavelength. Similar results are obtained for film deposited in oxygen atmosphere as shown in Fig. 4d.

Figure 5a, b shows the room temperature PL emission spectra for the $Y_2O_2S:Eu^{3+}$ films deposited in vacuum, argon and oxygen. All the samples were excited at 245 nm using a monochromatized xenon lamp. The luminescence display typical emission lines from the $^5D_0 \rightarrow {}^7F_J$ ($J = 0$–4) transitions of the Eu^{3+} ions. A distinct luminescence property of $Y_2O_2S:Eu^{3+}$ is the highest intensity of $^5D_0 \rightarrow {}^7F^2$ transition [32]. The main emission line of $Y_2O_2S:Eu^{3+}$ is at 612 nm as compared to 619 nm from commercially available $Y_2O_2S:Eu^{3+}$ for the same transition of $^5D_0 \rightarrow {}^7F_2$. Under the same measurement conditions ($\lambda_{ex} = 245$ nm), the intensity of commercial $Y_2O_2S:Eu^{3+}$ is about 1.3 (vacuum), 3.2 (argon) and 40 (oxygen) times higher than that of as-deposited $Y_2O_2S:Eu^{3+}$ films. A shoulder at 595 nm for the vacuum sample is also visible, which is ascribed to Eu^{2+} transitions. Minor emission peaks associated with residual Eu^{3+} [33, 34] was also observed at 402, 469, 496, 514 and 540 nm for the films deposited in the vacuum atmosphere. The relative ratios of the 595 nm to 613 nm peaks (Eu^{2+} to Eu^{3+} ratio) clearly support this observation. It should be mentioned that O_2 atmosphere should favor the stabilization of Eu^{3+} cations (oxidation), while vacuum should play the opposite role and favor Eu^{2+} (reduction). The intensity of the film deposited in the vacuum atmosphere was the highest followed by the one prepared in the argon atmosphere, though greatly quenched. All the peaks for the sample deposited in O_2 are totally quenched due to the smallest intensity as compared to that of vacuum and argon, hence not visible.

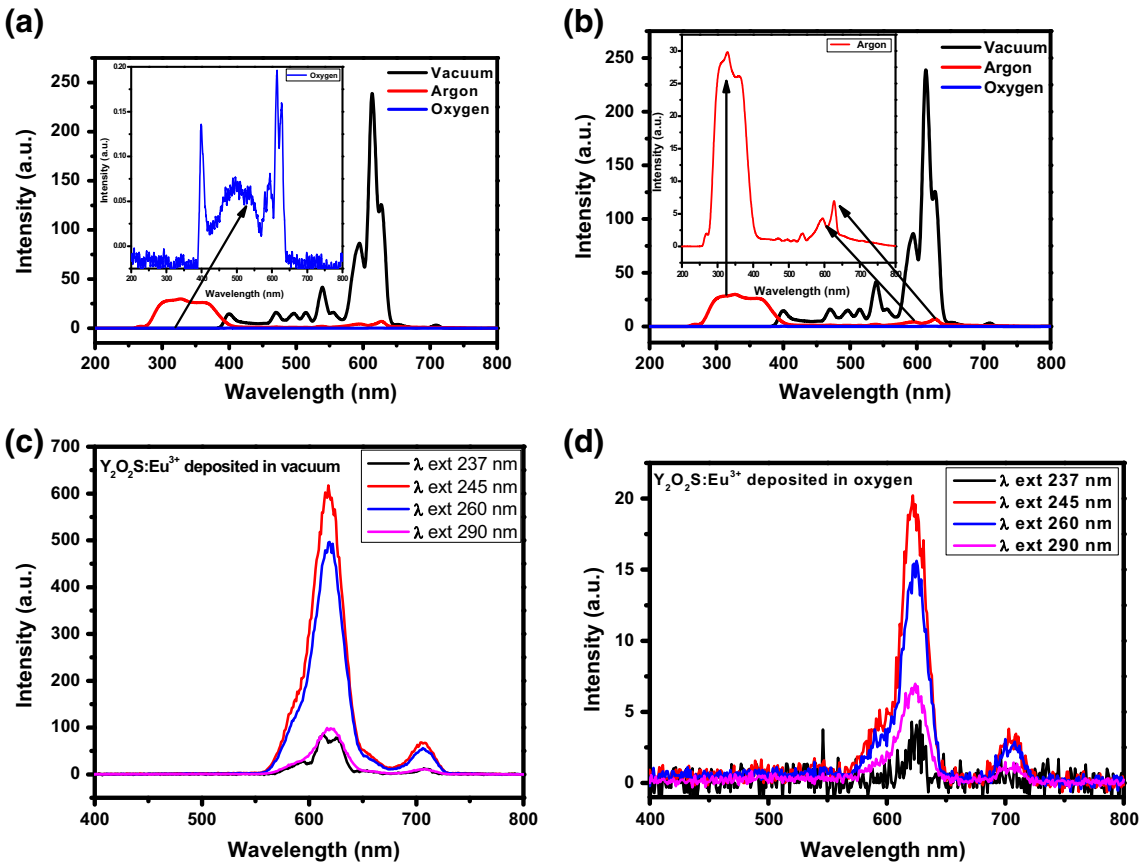

Fig. 5 **a** Emission spectra for $Y_2O_2S:Eu^{3+}$ thin films deposited in vacuum, argon and oxygen atmosphere. *Inset* Emission spectrum for thin film deposited in oxygen. **b** Emission spectra for $Y_2O_2S:Eu^{3+}$ thin films deposited in vacuum, argon and oxygen atmosphere. *Inset* Emission spectrum for thin film deposited in argon. **c** Emission spectra of $Y_2O_2S:Eu^{3+}$ thin film deposited in vacuum atmosphere recorded at 237, 245, 260 and 290 nm excitation wavelengths**. d** Emission spectra of $Y_2O_2S:Eu^{3+}$ thin film deposited in oxygen atmosphere recorded at 237, 245, 260 and 290 nm excitation wavelengths

But when PL emission spectra for sample deposited in O_2 are drawn alone, the peaks are clearly visible as shown in the inset of Fig. 5a. The most intense peak for this sample also appears exactly at 612 nm just as that of vacuum. In the case of film deposited in argon atmosphere, the peak at 612 nm is quenched, while that at 315 nm is enhanced. In all the three cases, the peak at 612 nm is associated with $O^{2-} \rightarrow Eu^{3+}$ charge transfer band (CTB) between O^{2-} and Eu^{3+} ions, while the peak at 315 nm is due to $Eu^{3+} \rightarrow S^{2-}$ charge transfer band. These peaks are clearly shown in Fig. 5b inset. A shift of the $Y_2O_2S:Eu^{3+}$ main peak toward shorter wavelengths was measured for sample deposited in argon atmosphere. This is due to the quantum size effect of the nanosized particles, compared with those deposited in vacuum and oxygen as confirmed by XRD results.

Figure 5c, d shows emission wavelengths for each film deposited in different gas atmospheres. In each case, the emission wavelengths were found at different excitation wavelengths in order to optimize emission for each film. Figures 5c indicates the emission wavelength for the film deposited in vacuum. At all, the excitation wavelengths of 237, 245, 260 and 290 nm, high-quality emission wavelength with high intensities, have been achieved with 245 and 260 nm excitation providing the highest intensity. Figure 5d indicates emission wavelengths for the film deposited in oxygen atmosphere. Similarly, the best emission wavelength was achieved when the excitation wavelength was at 245 and 260 nm, followed by 290 nm, respectively. The excitation wavelength with the least intensity is achieved at 237 nm excitation wavelength. The film deposited in oxygen atmosphere indicates the lowest intensity as shown in Fig. 5d at all excitations.

It is well known that the 613 nm peak due to the Eu^{3+} is much more pronounced than the 402–595 nm peak for thinner films (less laser pulses) [35, 36]. With all these in mind, it might be speculated at this stage that the shift in the emission wavelength of the Eu^{3+} emission in argon atmosphere might also be due to reduction in Eu^{3+} to Eu^{2+}. The crystal field due to different structures of cubic and hexagonal must also be kept in mind. The nanosize of the

particles formed during deposition also can play a role. The higher PL intensities from the films deposited in the vacuum atmospheres can be ascribed to the films' relatively rougher surface as observed from the AFM pictures in Fig. 3. It is well known that rough surfaces increase the probability of light emission from the surface by limiting the chances of total internal reflection at the film–substrate interface [37].

3.5 Decay curves

Figure 6 shows the decay characteristics of the thin films deposited in vacuum, O_2 and Ar atmospheres. Consistent with the PL data in Fig. 5, the film prepared in vacuum atmosphere has the highest initial intensity followed by the film prepared in the argon atmosphere. The fluorescence of $Y_2O_2S:Eu^{3+}$ is believed to originate from the photooxidation of Eu^{2+} cation under UV irradiation [38]. According to this model, an electron from the $^4f_7$ ground state is excited to the $^4f_6$–$^5d_1$ level of Eu^{2+} followed by an electron capture from the valence band reducing Eu^{2+} to Eu^{+}.

The films were further characterized by the fast and slow decays characteristics [39], since they are indicative of the different rates of decay for the films. The decay curves were fitted according to Eq. (3) and gave decay constants listed in Table 1.

$$I = A_1 \exp(-t/\tau_1) + A_2 \exp(-t/\tau_2) \quad (3)$$

where I is the phosphorescence intensity, A_1 and A_2 are constants, t is time, and τ_1 and τ_2 are decay times for exponential components, respectively. The fitting results of parameters t_1 and t_2 are listed in Table 1.

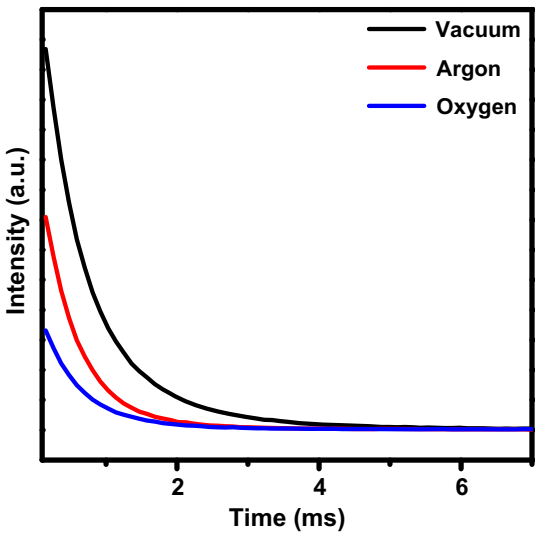

Fig. 6 Decay curves for PLD $Y_2O_2S:Eu^{3+}$ thin films deposited in vacuum and different gas atmospheres

It is clear from Table 1 that the decay constants for the vacuum and argon samples are longer than that of the oxygen sample. According to these results, the gas atmospheres did not play any role in the trap level concentration and also in the possible trap types.

3.5.1 Optical properties

3.5.1.1 Reflectance spectra The UV–Vis reflectance spectra of the samples are given in Fig. 7. The spectra of all the samples show good optical quality in the visible range due to the complete reflectance in the 200–500 nm range. The sharp absorption edge is characteristic of a homogeneous structure [40]. The figure shows that the absorption edge shifted to higher wavelength in the order vacuum, argon and oxygen. Absorption bands corresponding to the forbidden Eu^{3+} 4*f*–4*f* transitions were also detected for film deposited in O_2. The band at around 343 nm is attributed to the exciton absorption, which is redshift compared with powder $Y_2O_2S:Eu^{3+}$ [41]. The absorption peaks at around 290 and 340 nm are assigned to $^5D_0$–$^7F_1$ and $^5D_0$–$^7F_2$ transitions of Eu^{3+} ions, respectively [42].

3.5.1.2 Determination of band gap from reflectance spectra The Kubelka–Munk equation was used to calculate the band gap of the as-deposited thin film using a diffuse reflectance spectrum. The bang gap (Eg) and absorption coefficient ∝ of direct band gap semiconductor are related through the Tauc relation. By plotting $[F(R) \times hv]^2$ against hv and fit the linear region with a line and extending it to the energy axis, then one can easily obtain Eg by extrapolating the linear regions to $[F(R) \times hv]^2 = 0$.

The dependence of the band gap energy of the Y_2O_2S on the vacuum and different gas species is shown in Fig. 8. The observed optical band gap for $Y_2O_2S:Eu^{3+}$ thin films increased in the order vacuum (3.4 eV), argon (4.3 eV) and oxygen (4.4 eV) as shown in Fig. 8. The average Eg value for the thin films was found to be 4.07 eV, which is in a good agreement with the literature values by other researchers [43]. The change in optical band gap values may also be due to the change of crystal structure of the Y_2O_2S thin films (hexagonal verse cubic). This is also confirmed by the fact that the PL emission intensity of the films deposited in vacuum is more than 5 times greater than the intensity of $Y_2O_2S:Eu^{3+}$ thin films deposited in gas atmosphere.

The increase in band gap energy and the shift of the absorption edges to higher wavelengths in the case of film deposited in gas atmosphere might be due to the presence of defect states and disorder due to the different deposition atmospheres [44]. The gas atmospheres might have introduced new states close to the conduction band of the $Y_2O_2S:Eu^{3+}$. A new defect band is therefore formed below

Table 1 Decay constants for the fitted decay curves of the thin films ablated in vacuum, argon and oxygen atmospheres

Atmosphere Components	Vacuum Decay constants(τ, s)	Argon	Oxygen
Fast (τ_1)	0.475 (1) ± 0.002 (4)	0.474 (9) ± 0.007 (4)	0.468 (2) ± 0.001 (9)
Medium (τ_2)	0.657 (3) ± 0.006 (4)	0.618 (4) ± 0.006 (7)	0.586 (5) ± 0.005 (5)

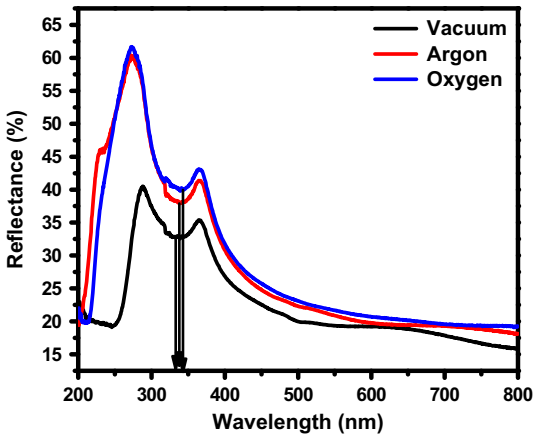

Fig. 7 UV–Vis diffuse reflectance spectra of nanocrystalline $Y_2O_2S:Eu^{3+}$ thin film deposited in vacuum, argon and oxygen atmospheres

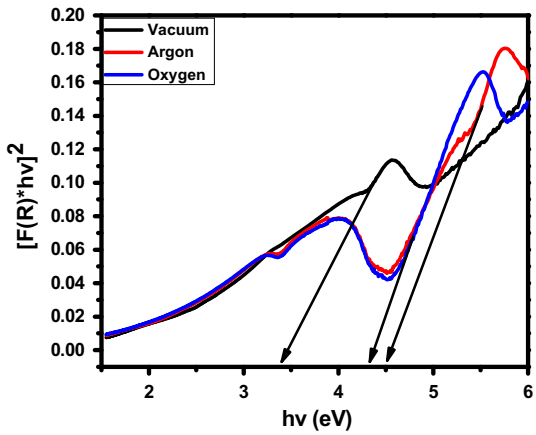

Fig. 8 Graph of $F[(R) \times hv]^{1/2}$ as a function of band gap energy

the conductions which lead to reduction in the effective band gap [45].

4 Conclusion

Red-emitting $Y_2O_2S:Eu^{3+}$ thin-film phosphors were successfully ablated on Si (100) substrates by the pulsed laser deposition technique. The X-ray diffraction patterns showed mixed phases of cubic and hexagonal crystal structures. The SEM micrographs show that the surfaces of the films prepared in the gas atmosphere are much rougher than that deposited in vacuum. Intense red emission, with a maximum peak at 612 nm associated with the $^5D_0$–$^7F_2$ transitions of Eu^{3+}, was detected from the films deposited in vacuum and argon atmosphere. The working atmosphere has a severe influence on the PL properties of the films. The films deposited in the vacuum atmospheres gave better PL and afterglow properties than the film prepared in gas atmospheres. The crystallinity and PL properties of the sample ablated in vacuum gave the best bright red emission. UV–Vis measurement gave an average band gap of 4.07 eV.

References

1. P. Sharma, D. Haranath, H. Chander, S. Singh, Appl. Surf. Sci. **254**, 4052 (2008)
2. W.W. Zhang, W.P. Zhang, P.B. Xie, M. Yin, J. Colloid Interface Sci. **262**(2003), 588 (2003)
3. Y.Q. Zhai, Z.H. Yao, S.W. Ding, M.D. Qiu, J. Zhai, Mater. Lett. **57**, 2901 (2003)
4. H.S. Peng, H.W. Song, B.J. Chen, S.Z. Lu, S.H. Huang, Chem. Phys. Lett. **370**, 485 (2003)
5. T. Hirai, Y. Asada, I. Komasawa, J. Colloid Interface Sci. **276**, 339 (2004)
6. J. Hao, S.A. Studenikin, M. Cocivera, J. Lumin. **93**, 313 (2001)
7. L.P. Wang, G.Y. Hong, Mater. Res. Bull. **35**, 695 (2000)
8. J.P. Lang, X.Q. Xin, J. Solid State Chem. **108**, 118 (1994)
9. H.T. Cui, G.Y. Hong, H.P. You et al., J. Colloid Interface Sci. **252**, 184 (2002)
10. R.K. Singh, J. Narayan, Phys. Rev. B **41**, 8843 (1991)
11. A. Gupta, in *Pulsed Laser Deposition of Thin Films*, ed. by D.B. Chrisey, G.K. Hubbler (Wiley, New York, 1994), p. 265
12. A. Greer, M. Tahal, Mater. Res. Soc. Symp. Proc. **341**, 87 (1994)
13. S.S. Yi, J. Korean Phys. Soc. **45**, 1625 (2004)
14. J.S. Bae, K.S. Shim, B.K. Moon, S.B. Kim, J.H. Jeong, S.S. Yi, J.H. Kim, J. Korean Phys. Soc. **46**, 1193 (2005)
15. S.-D. Han, K.C. Singh, T.-Y. Cho, H.-S. Lee, D. Jakhar, J.P. Hulme, C.-H. Han, J.-D. Kim, I.I.-S. Chun, J. Gwak, J. Lumin. **128**, 301 (2008)
16. Y.-L. Chang, H.-I. Hsiang, M.-T. Liang, J. Alloys Compd. **461**, 598 (2008)
17. P.D. Sarkisov, N.V. Popovich, A.G. Zhelnin, Glass Ceram. **60**, 9 (2003)
18. T. Peng, L. Huajun, H. Yang, J. Mater. Chem. Phys. **85**, 68 (2004)
19. T. Peng, H. Yang, X. Pu, B. Hu, Z. Jian, C. Yan, Mater. Lett. **58**, 352 (2004)
20. X. Li, Y. Qu, X. Xie, Z. Wang, R. Li, Mater. Lett. **60**, 3673 (2006)
21. D.P. Norton, Mater. Sci. Eng., R **43**, 139 (2004)
22. E. Arimondo, F. Calderazzo, F. Fuso, G. Masciarelli, C. Toffi, Appl. Phys. A **66**, 487 (1998)
23. A. Bailini, P.M. Ossi, A. Rivolta, Appl. Surf. Sci. **253**, 7682 (2007)

24. A. Dauscher, M. Puyet, B. Lenoir, D. Colceag, M. Dinescu, Appl. Phys. A **79**, 1465 (2004)
25. S. Choopun, H. Tabata, T. Kawai, J. Cryst. Growth **274**, 167 (2005)
26. S. Som, S.K. Sharma, S.P. Lochab, Phys. Status Solidi A **210**, 1624–1635 (2013)
27. B.D. Cullity, *Elements of X-Ray Diffraction*, 2nd edn. (Addison-Wesley, Reading, 1978), p. 312
28. E. Coetsee, H.C. Swart, J.J. Terblans, O.M. Ntwaeaborwa, K.T. Hillie, W.A. Jordaan, U. Buttnerk, Opt. Mater. **29**, 1338 (2007)
29. S.S. Kim, B.-T. Lee, Thin Solid Films **446**, 307 (2004)
30. L. Chen, Particles generated by pulsed laser ablation. in *Pulsed Laser Deposition of Thin Films* ed. by D.B. Chrisey, G.K Hulber (Wiley, New York, 1994) chap. no. 6, p. 167, 184
31. K. Sato, S. Komuroa, T. Morikawa, H. Aizawa, T. Katsumata, S. Harako, X. Zhao, J. Cryst. Growth **275**, 1137 (2005)
32. P.D. Nsimama, O.M. Ntwaeaborwa, E. Coetsee, H.C. Swart, Phys. B. Condens. Matter **404**, 4489 (2009)
33. O.M. Ntwaeaborwa, P.D. Nsimama, S. Pitale, I. Nagpure, V. Kumar, E. Coetsee, J.J. Terblans, H.C. Swart, P.T. Sechogela, J. Vac. Sci. Technol., A **28**, 901 (2010)
34. O.M. Ntwaeaborwa, P.D. Nsimama, J.T. Abiade, E. Coetsee, H.C. Swart, Phys. B: Phys. Condens. Matter **404**, 4436 (2009)
35. D. Jia, Opt. Mater. **22**, 65 (2003)
36. H.K. Yang, K.S. Shim, B.K. Moon, B.C. Choi, J.H. Jeong, S.S. Yi, J.H. Kim, Thin Solid Films **516**, 5577 (2008)
37. J.S. Kim, J. Ceram. Proc. Res. **10**, 443 (2009)
38. F. Clabau, X. Rocquefelte, S. Jobic, P. Denieard, M.-H. Whangbo, A. Garcia, T. Mercier, Solid State Sci. **9**, 608 (2007)
39. D. Zang, Y. Zhinong, W. Xue, T. Zhang, Z. Ding, W. Wang, J. Rare Earths **28**, 185 (2010)
40. J.S. Kim, J. Ceram. Proc. Res. **10**, 443 (2009)
41. L. Luan, C.F. Guio, D.X. Huang, J. Inorg. Mater. **24**, 53 (2009)
42. Y.Q. Li, N. Hirosaki, R.-J. Xie, M. Mitomo, Sci. Technol. Adv. Mater. **8**, 607 (2007)
43. C. Chang, Z. Yuan, D. Mao, J. Alloys Compd. **415**, 220 (2006)
44. S.L. Jones, D. Kumar, K.-G. Cho, R. Singh, P.H. Holloway, Displays **19**, 151 (1999)
45. F. Clara, X. Rocquefelte, S. Jobic, P. Deniard, M.H. Whangbo, A. Garcia, T.L. Merciesr, Chem. Mater. **17**, 3909 (2005)